Microscopic Imaging of Slow Flow and Diffusion: A Pulsed Field Gradient Stimulated Echo Sequence Combined with Turbo Spin Echo Imaging

T. W. J. Scheenen, F. J. Vergeldt, C. W. Windt, P. A. de Jager, and H. Van As[1]

Laboratory of Biophysics, Department of Agrotechnology and Food Sciences, Wageningen University,
Dreijenlaan 3, 6703 HA Wageningen, The Netherlands

E-mail: Henk.Vanas@water.mf.wau.nl

In this paper we present a pulse sequence that combines a displacement-encoded stimulated echo with rapid sampling of k-space by means of turbo spin echo imaging. The stimulated echo enables the use of long observation times between the two pulsed field gradients that sample q-space completely. Propagators, constructed with long observation times, could discriminate slowly flowing protons from diffusing protons, as shown in a phantom in which a plug flow with linear velocity of 50 μm/s could clearly be distinguished from stationary water. As a biological application the apparent diffusion constant in longitudinal direction of a transverse image of a maize plant stem had been measured as a function of observation time. Increasing contrast in the apparent diffusion constant image with increasing observation times were caused by differences in plant tissue: although the plant stem did not take up any water, the vascular bundles, concentrated in the outer ring of the stem, could still be discerned because of their longer unrestricted diffusional pathways for water in the longitudinal direction compared to cells in the parenchymal tissue. In the xylem region of a tomato pedicel flowing water could be distinguished from a large amount of stationary water. Linear flow velocities up to 0.67 mm/s were measured with an observation time of 180 ms. © 2001 Academic Press

Key Words: **MRI; dynamic NMR microscopy; T_1; PFG; STE; TSE; RARE.**

INTRODUCTION

Already in 1965 Stejskal and Tanner demonstrated that pulsed magnetic field gradients (PFGs) could be used in nuclear magnetic resonance (NMR) to probe the displacement of protons in a sample (*1*). Their well-known equation describes the attenuation of the normalized NMR signal $S(\mathbf{g})$ of diffusing protons as a function of amplitude ($\mathbf{g}$), spacing (Δ), and duration (δ) of the two PFGs, and as a function of the diffusion constant D of the protons,

$$S(\mathbf{g})/S(0) = \exp(-\gamma^2 \mathbf{g}^2 \delta^2 D(\Delta - \delta/3)), \qquad [1]$$

where γ is the gyromagnetic ratio of protons. Apart from the NMR signal amplitude attenuation as a result of diffusion, the phase of the NMR signal shifts when the protons move in the direction of the PFGs during Δ. Kärger and Heink measured the NMR signal as a function of the intensity m of the PFGs in one direction ($m = \gamma \delta \mathbf{g}$, also known as **q**-space with $\mathbf{q} = \gamma \delta \mathbf{g}/2\pi$ (*2*)), and Fourier transformed the complex NMR signal as a function of m into the averaged propagator $P(R, \Delta)$ (*3*). An averaged propagator is a spectrum representing the distribution of spin displacements (R) in the direction of the PFGs within Δ.

Probing displacements with PFGs can be combined with imaging to construct propagators for every pixel in an image (*2, 4–6*). Pixel propagators can represent different proton pools. In transverse images of plant stems for instance, pixels in the xylem tissue that transports water from roots to shoot and leaves can contain flowing water in a xylem vessel surrounded by stationary water outside the vessel (*6, 7*). The pixel propagator will show stationary water as a symmetrical part of the displacement distribution centered at zero displacement and flowing water as a part of the displacement distribution with a net displacement (cf. Fig. 1c). Recently a method for quantifying the flowing part of the propagator of every pixel in an NMR image without assuming any model for the flow profile of the flowing water has been presented (*7*), in contrast to fitting a model function to the NMR signal modulation by a number of q-steps, assuming the occurrence of one complete laminar flow profile in one pixel (*8–10*).

With both quantification methods, problems arise when one wants to study slow flow: one needs long observation times (Δ) to distinguish between displacements originating from slow flow and displacements originating from free diffusion. This will be evident from the following discussion. The root mean square (rms) displacement σ due to diffusion, observed by NMR, is proportional to the square root of the corrected observation time $\Delta - \delta/3$,

$$\sigma = \sqrt{2D(\Delta - \delta/3)}, \qquad [2]$$

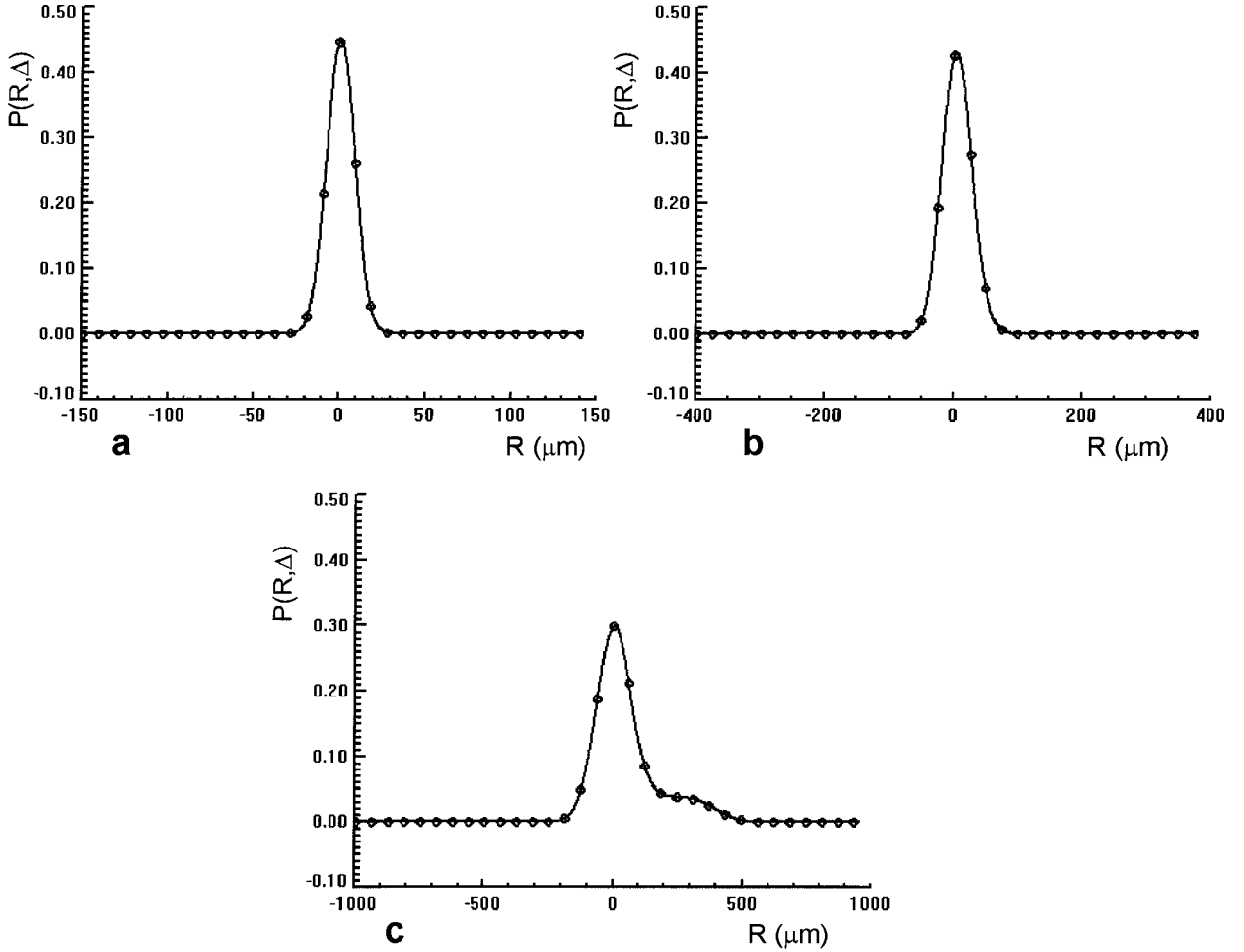[1] To whom correspondence should be addressed. Fax: (31)-317-482725.

FIG. 1. Three simulated propagators of 75% stationary water and 25% flowing water. The diffusion constant of the stationary and flowing water is 2.20×10^{-9} m^2/s, the mean linear flow velocity of the flowing water is 200 μm/s. No exchange between stationary and flowing water and no radial diffusion over the laminar flow profile have been assumed. Δ values are (a) 15, (b) 100, and (c) 1000 ms. The solid lines are the calculated propagators; the symbols indicate the sampling of the propagator with a hypothetical experiment with 32 PFG steps.

whereas the mean displacement $\bar{r}$ of flowing protons is proportional to Δ itself,

$$\bar{r} = \bar{v}\Delta, \qquad [3]$$

in which $\bar{v}$ is the mean flow velocity of the flowing protons. Suppose one wants to distinguish water, flowing with a laminar flow profile at a mean velocity of 200 μm/s, from stationary water at 20°C (D of free water at 20°C is 2.20×10^{-9} m^2/s, no exchange between flowing and stationary water, volume fraction flowing water 0.25, $\delta \ll \Delta$). With a Δ of 15 ms $\bar{r}$ would be 3.0 μm, whereas σ would be 8.1 μm, which makes a distinction between flow and diffusion hardly possible (Fig. 1a) on the basis of displacements. Going up to 100 ms observation time $\bar{r}$ and σ would be 20 and 21 μm respectively (Fig. 1b), and at a value of Δ of 1 s, $\bar{r}$ and σ become 200 and 66 μm. In this last case the flowing part of the propagator becomes clearly visible (Fig. 1c). Transversal diffusion of the water is accounted for in these theoretical examples but radial diffusion, perpendicular

to the flow direction, is neglected. Incorporating radial diffusion would mean that water molecules move across the laminar, parabolic flow profile, changing the shape of the propagator and decreasing the already small maximum displacement of the flowing water, although $\bar{r}$ would remain unaffected (11).

If long observation times are used in PFG experiments, the time from signal excitation to detection of the first echo will also be long. In this case the need for a stimulated echo (STE) sequence, instead of a spin echo (SE) sequence emerges. Already in 1985 the STE had been used in an imaging sequence (12) and was soon combined with PFGs to measure diffusion (13) and flow (14). Since T_1 is always (often substantially) longer than T_2, it is advantageous or even necessary during long observation times to store the magnetization along the z axis, where magnetization can evolve according to T_1: despite the inherent loss of a factor of 2 in signal-to-noise ratio (SNR) in an STE amplitude, this amplitude can still be larger than an SE amplitude. Recording a complete set of pixelpropagators with only

one echo per scan is very time-consuming (*4, 5*). In order to decrease the total acquisition time, we combined the STE with a turbo spin echo (TSE) train. The displacement-encoded STE is modulated in the TSE train to obtain a TSE image for every displacement-encoding step. Since an STE pulse sequence also generates spin echoes (SE of first and second 90° pulses, SE of second and third 90° pulses (*15*), SE of first and third 90° pulses, and SE of first SE and third 90° pulse), a 180° pulse train behind a STE can also refocus these spin echoes, producing unwanted spurious echoes in the echo train, resulting in image ghosting. With appropriate phase schemes and spoiler gradients all spurious echoes are suppressed and acceptable TSE images can be obtained. As challenging applications of the STE TSE sequence we measured slow flow in a pedicel of a tomato and constructed images of the apparent diffusion constant of a transverse slice of a maize plant stem as a function of observation time Δ.

THE PULSE SEQUENCE

Figure 2 shows an outline of the *p*ulsed *f*ield *g*radient *st*imulated *e*cho *t*urbo *s*pin *e*cho (PFG STE TSE) pulse sequence. Like its SE variant (*6*) this sequence uses PFGs to encode for displacement and the turbo spin echo technique, also known as fast SE or RARE (*16*), to shorten imaging time. The difference is the use of a STE to store magnetization along the *z* axis during Δ. As in the SE version we were able to maintain a coherent amplitude and phase throughout the echo train, so amplitude and phase information, encoded with the PFGs, could be recorded throughout the TSE train.

After the first slice-selective $90°_x$ pulse the magnetization in the *xy* plane is displacement-encoded with the first PFG. All spins in the coil experience the second, hard, $90°_x$ pulse that stores half the magnetization of those spins, which experienced the first RF pulse, along the *z* axis for a time t_{mid}. All residual magnetization in the *xy* plane (FID of hard pulse) is crushed with the spoiling gradient g_{spoil}. After the third, hard $90°_x$ pulse that will induce the STE, displacement encoding is completed with the second PFG. The FID of the third $90°_x$ pulse is crushed with the crusher pairs in the phase encode and readout direction and with the second PFG. All gradient pulses in the sequence are ramped; in calculating the effective duration δ of the stepped PFGs (amplitudes from $-g_{max}$ to 0 to $+g_{max-1}$), one ramp of 100 μs is included. Possible extra signal attenuation due to diffusion between readout gradients or crushers and differences in T_1 and T_2 in the sample will not vary as a function of PFGs, so the shape of the constructed propagators will only be determined by displacements of the spins involved. The TSE train after the STE phase-encodes every echo between the hard 180° pulses individually, unwrapping the phase-encoded gradient after every echo. Since the magnetization in the *xy* plane is encoded for displacement with the PFGs, the phase of the signal can have any value between minus and plus π, depending on $\gamma \delta \mathbf{g}$ and the displacement of the observed spins within the labeling time. Alsop (*17*)
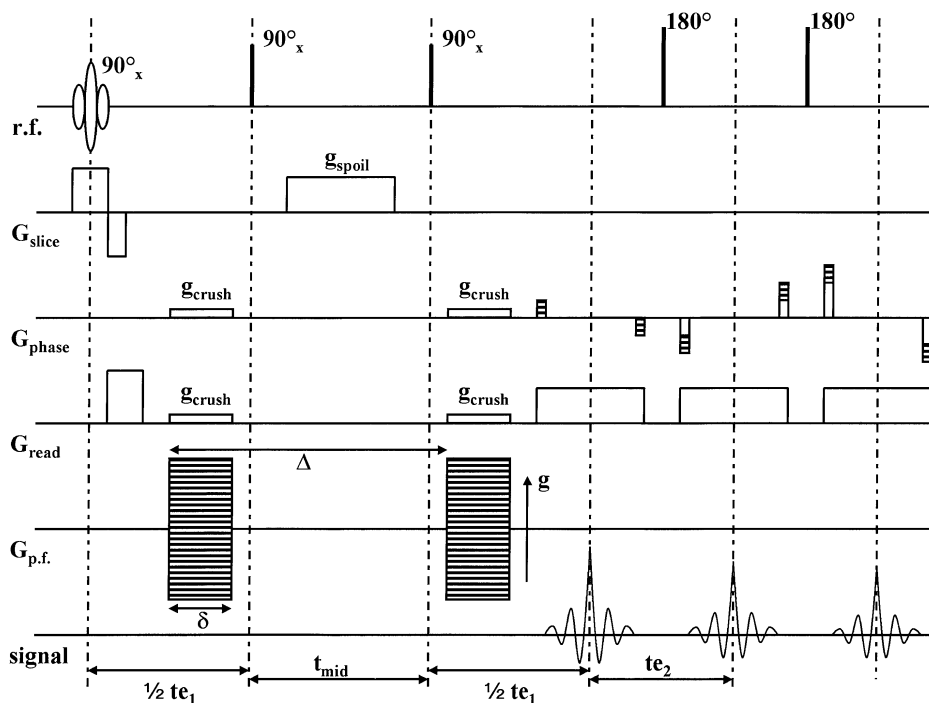

FIG. 2. An outline of the *st*imulated *e*cho *p*ulsed *f*ield *g*radient *t*urbo *s*pin *e*cho (STE PFG TSE) pulse sequence. A large spoiling gradient during t_{mid} crushes magnetization in the *xy* plane after the first two 90° pulses, whereas the crushers (g_{crush}) and the second PFG within the second $1/2$ te$_1$ period crush the free-induction decay of the third 90° pulse.

described the problems of refocusing prepared magnetization in a multiple-spin-echo train and pointed out that it is crucial either to use pulses in the pulse train with flip angles as close to 180° as possible or to modify the TSE part of the sequence in gradient and RF pulse amplitudes to prevent rapid signal amplitude decay and oscillations. Edzes *et al.* (*18*) reported on the accuracy of observed T_2 values in images of plant tissues (magnetization preparation with a phase encode gradient) within 3% of its proper values as long as the 180° pulses were accurate within ±5°. By interactively adjusting the RF pulse amplitude, observing the pulse profile in the solenoid RF coil we were able to set and keep the refocusing pulses in the center of the coil at their correct value. The TSE part of the sequence, including the MLEV-4 phase scheme of the 180° RF pulses and the k-space trajectories of the echoes, is described elsewhere, including the signal processing of the data into pixel propagators for every pixel in an image (*6*).

PHANTOM STUDY

To check whether this technique to construct pixel propagators with long observation times is able to distinguish very slow flow from self-diffusion we measured the propagators of a phantom with stationary and slowly flowing water. Inside a glass tube with doped (0.1 mM $MnCl_2$) water was another tube through which a capillary, filled with doped water, was pulled upward with a syringe pump (model YA-12, Yale Apparatus, Wantagh NY, USA). This created a perfect plug flow with a controlled and well-defined flow velocity (50.0 ± 0.2 μm/s) surrounded by stationary water.

The phantom was fixed in a dedicated solenoid RF coil (~19 mm inner diameter) inside a custom-engineered gradient probe (Doty Scientific Inc., Columbia, SC, USA), controlled with an SMIS console (Surrey Medical Imaging Systems Ltd., Guildford, Surrey, UK). The 0.7-T magnetic field was generated

with an electromagnet (Bruker, Karlsruhe, Germany), stabilized by the use of an external ^{19}F lock unit (SMIS).

Figure 3a shows an image of the water density of the phantom. This image is constructed by fitting a monoexponential decay curve to the NMR signal of every pixel in an echo train to calculate the NMR signal intensity at the moment of excitation (*18*). From a PFG STE TSE experiment we also constructed the propagator in the direction of the plug flow for every pixel of the image of the phantom. Because displacements of protons in the phantom in the direction of the PFGs are unrestricted, all pixel propagators (including pixels inside the moving capillary) were subject to a nonlinear least-squares fit to a Gaussian function with amplitude A

$$P(R, \Delta) = A \exp\left(-\left(\frac{R - \bar{r}}{\sigma}\right)^2 \bigg/ 2\right), \qquad [4]$$

using the Levenberg–Marquardt method (*19*). Figures 3b and 3c reflect the results of the Gaussian fit: an image of the position of the maximum of the fitted Gaussian (Fig. 3b), representing the mean displacement $\bar{r}$ of the water of the corresponding pixel and the diffusion constant D (Fig. 3c), calculated from σ by Eq. [2]. Using Eq. [3], $\bar{r}$ can be used to calculate $\bar{v}$. In Fig. 3a two groups of pixels are indicated: 16 pixels in the center of the capillary and 49 pixels in the large tube. The mean values for $\bar{v}$ and D are 51 ± 8 μm/s and 2.6 ± 0.1 × 10^{-9} m^2/s for the pixels indicated inside the capillary. For the indicated pixels in the large tube $\bar{v}$ and D are 0 ± 7 μm/s and 2.6 ± 0.1 × 10^{-9} m^2/s respectively (given errors are standard deviations). The linear flow velocity of the water in the capillary (51 ± 8 μm/s) coincides with the velocity with which the capillary was pulled upward with the syringe pump (50.0 ± 0.2 μm/s), although the standard deviation of the velocity is large (16%) due to a low signal-to-noise ratio of the experiment. The diffusion constant

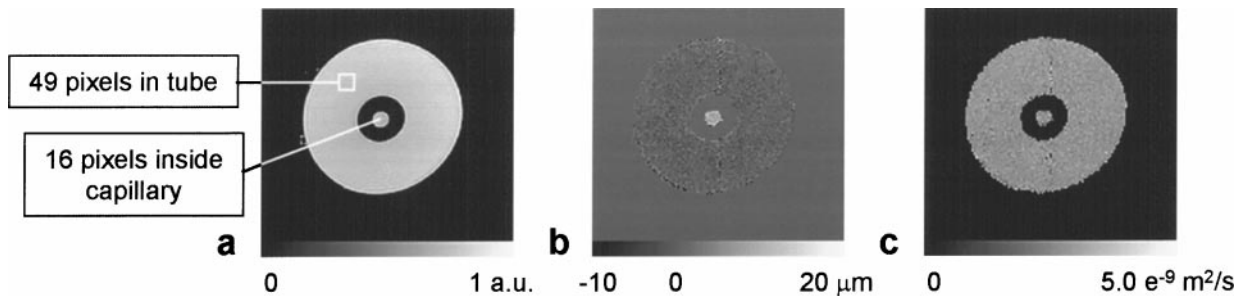**FIG. 3.** Images of a phantom with stationary water and water in a capillary that is pulled through an empty tube at a velocity of 50.0 μm/s. (a) Calculated image of the initial signal amplitude. (b) The position of the maximum of the Gaussian fit to the propagator of every pixel: the mean displacement $\bar{r}$ of the water. (c) The diffusion constant D, calculated from the characteristic width σ of the Gaussian fit (Eq. [2]). The grayscale bar in every image represents the indicated quantitative values for the different variables. Since the calculated initial NMR signal amplitude is in arbitrary units, no values are indicated in (a). Also in (a) the pixels used to calculate the mean values and standard deviations of those in the capillary and those in the large tube containing stationary water are pointed out. Mean T_2 inside the capillary is 143 ± 5 ms; mean T_2 in the large tube is 143 ± 2 ms. Experimental parameters: 128 × 128 matrix, field of view 20 mm, slice thickness 3.0 mm, repetition time 2 s. Extra parameters (a): echo time in train, 4.8 ms; 64 echoes, measurement time, 17 min. Extra parameters (b) and (c): 32 PFG steps; Δ, 150.1 ms; δ, 1.5 ms; PEG_{max}, 0.217 T/m; echo time in train, 4.4 ms; 32 echoes in TSE train; measurement time, 19 min.

of the water inside the capillary is equal to that of the water in the tube: the D values correspond to a sample temperature of 31°C.

MAIZE PLANT STEM

To test the pulse sequence with a biological sample a water-cultured maize plant stem was cut from its roots and put in the instrumental setup. Because of the air inlet during cutting the maize plant did not take up any water. The strength of the technique is the possibility of using long displacement encoding times, so to study the longitudinal diffusion constant for every pixel in an image of the stem, propagators in the direction along the plant stem were constructed with the following series of Δ values: 15.1, 30.1, 50.1, 100.1, 175.1, 250.1, and 400.1 ms. Since the diffusional pathways of the water in the cells are restricted by the boundaries or membranes from the different cell compartments the measured D depends on Δ and is now defined as

the apparent diffusion constant (ADC). In Figs. 4d to 4j images of the calculated ADCs as a function of Δ are presented, next to images of the calculated water density (Fig. 4a) and the T_2 (Fig. 4b) of the maize plant stem. Figure 4c is an optical micrograph of a different maize plant stem as an anatomical reference (after (20), p. 418). The stem, below the apex, consists of homogeneous tissue of large parenchymal cells and scattered vascular bundles, visible in the water density image as high intensity dots, and in the T_2 image as dots with T_2 values smaller than those of parenchymal tissue. The majority of the vascular bundles is concentrated in the outer ring of the stem, clearly visible as a ring with smaller T_2 values in comparison with parenchymal tissue. In the NMR images two leaves embrace the stem. A reference capillary with doped water is clearly visible in the calculated water content image, but with a mean T_2 of 21 ± 2 ms (22 pixels in capillary) it is almost invisible in the T_2 image. In the series of ADC images the reference capillary can be discerned up to
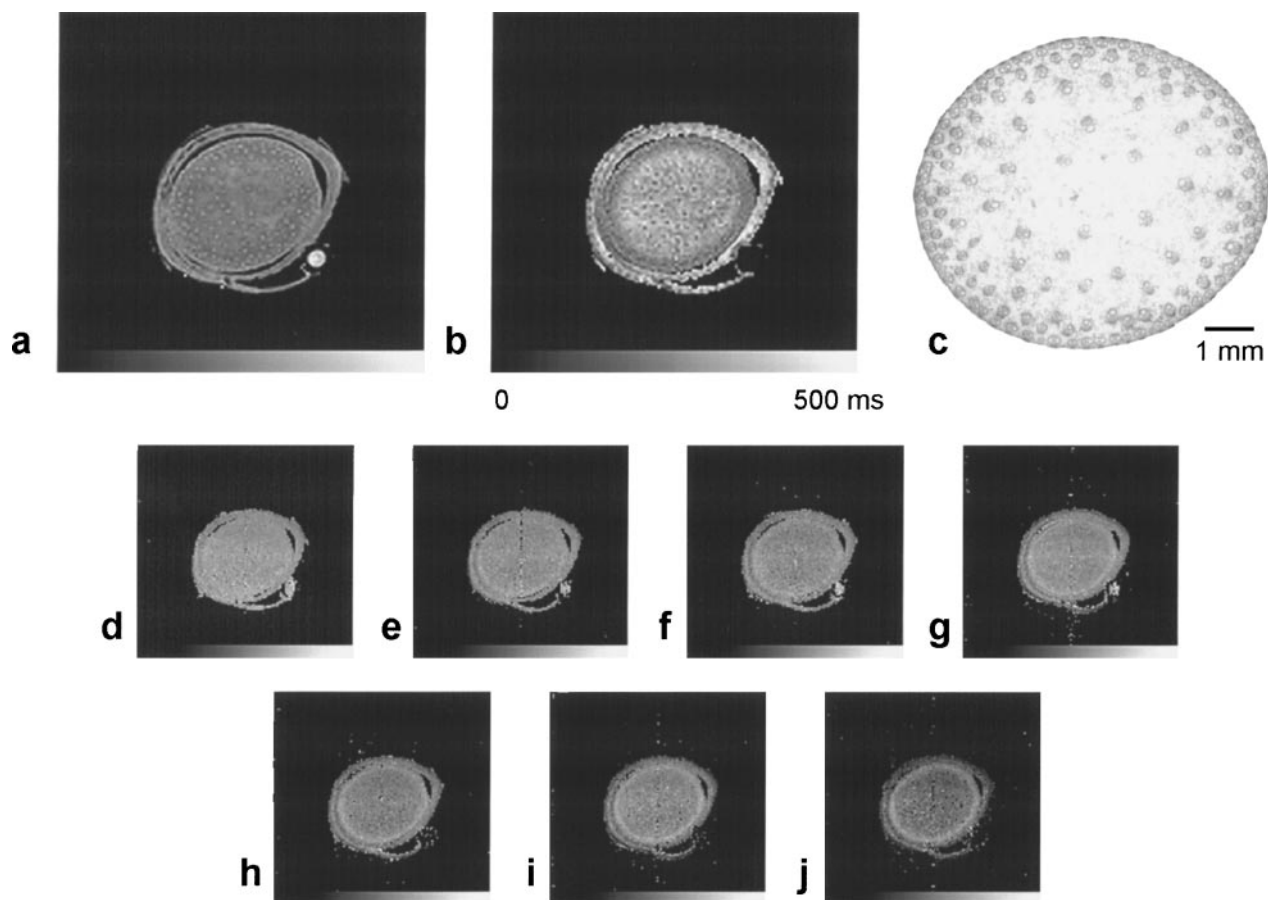

FIG. 4. Cross-sectional images of the maize plant stem, measured below the apex in the regions where the stem tissue consists of homogenous parenchymal tissue and scattered vascular bundles: (a) Calculated water content image, (b) calculated T_2 image, (c) microscopic picture of a transverse coupe of a maize plant stem without stem embracing leaves (after (20), p. 418), (d–j) Images of the calculated (Eq. [2]) apparent diffusion constant (ADC, in longitudinal direction, along the plant stem) as a function of the following Δ values: 15.1, 30.1, 50.1, 100.1, 175.1, 250.1, and 400.1 ms. The grayscale bar in image (b) reflects the indicated T_2 values quantitatively, the bars in images (d–j) indicate ADC values from 0 to 4.0×10^{-9} m²/s. Parameters for (a, b) are as described for Figs. 3a and 3b. Parameters for (d–j) are as described for Figs. 3c and 3d, but for every Δ value, δ, PFG$_{max}$, and measurement time (averaging) have been adjusted to sample **q**-space correctly with a sufficient signal-to-noise ratio. Measurement time ranges from 34 to 102 min. for Δ being 15.1 to 400.1 ms, respectively.

Mean Value and Standard Deviation of the Apparent Diffusion Constant of 22 Pixels in the Reference Capillary Next to the Maize Plant Stem as a Function of the Observation Time Δ

	$\Delta = 15.1$ ms	$\Delta = 30.1$ ms	$\Delta = 50.1$ ms	$\Delta = 100.1$ ms
D (10^{-9} m^2/s)	2.8 ± 0.2	2.8 ± 0.7	3.0 ± 0.4	3.0 ± 0.5

a Δ value of 100.1 ms, which is about five times the T_2 value. The mean value for the ADC in the reference capillary does not change as a function of Δ, although the standard deviation of the ADC increases because of the decreasing signal-to-noise ratio as the time from the first RF pulse to the STE increases (see Table 1): because diffusion is unrestricted, the ADC will resemble the intrinsic D of the water in the capillary.

In the plant stem hardly any contrast in ADCs can be seen at small Δ values (images 4d and 4e), but as Δ increases, some contrast between the center of the stem and the peripheral ring, which is also visible in the T_2 image, becomes clear. Actually, ADC values of all pixels in the stem decrease, which is even more evident in the histogram in Fig. 5, in which the amount of pixels that have a certain ADC are plotted versus the ADC itself for three Δ values. The ADC distribution becomes broader with a decreasing mean value: when Δ is small, water molecules will not meet restrictions in their vicinity so the ADC resembles the intrinsic D of the corresponding molecules. When Δ is larger, the chance that a water molecule will be restricted in its diffusional pathway gets larger and the ADC decreases. Tissue with small cells or cell compartments will impose more restrictions on the diffusing water molecules than larger cells or cell compartments, which is an origin of contrast in the ADC.
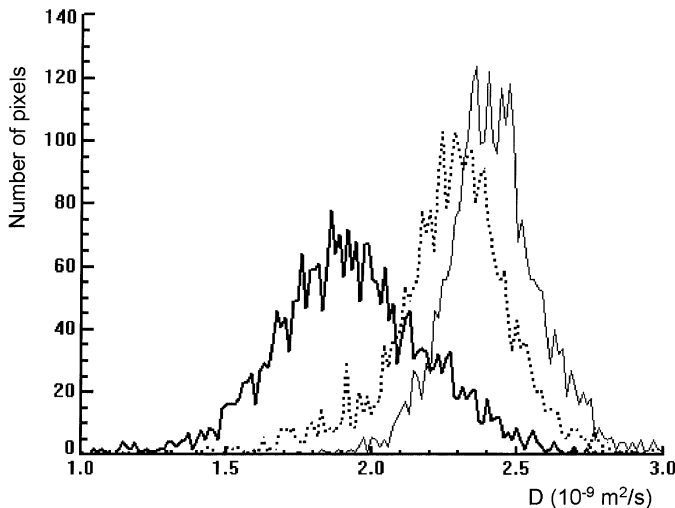
Differences in cell size and cell compartment sizes in the maize stem are why the ADC histogram broadens with increasing Δ. The ADC of pixels in the peripheral ring with mainly vascular bundles and of pixels containing scattered vascular bundles in the parenchymal tissue does not decrease as much as the ADC of pixels in the parenchymal tissue itself: vascular bundles have longer unrestricted diffusional pathways in the longitudinal direction than cells in the parenchymal tissue have. T_2 values of the peripheral ring and the scattered vascular bundles are smaller than T_2 values in parenchymal tissue (cf. the T_2 image in Fig. 4b) but, as mentioned earlier, differences in T_2 of different tissues in the stem are not reflected in the ADCs of the corresponding tissues. Relaxation times have been linked to diffusion constants in a (time-consuming) PFG experiment in which the echo train is not used for fast imaging, but for calculating T_2 values (21). Combining an echo train for calculating T_2 values with measuring the propagator for every pixel would also take a lot of acquisition time, but it could link different T_2 values to different displacements (either due to flow or diffusion) of the water for every pixel.

PEDICEL OF A TOMATO

The final application presented here is the measurement of a small pedicel of a tomato. We cut off a pedicel (21 mm length,
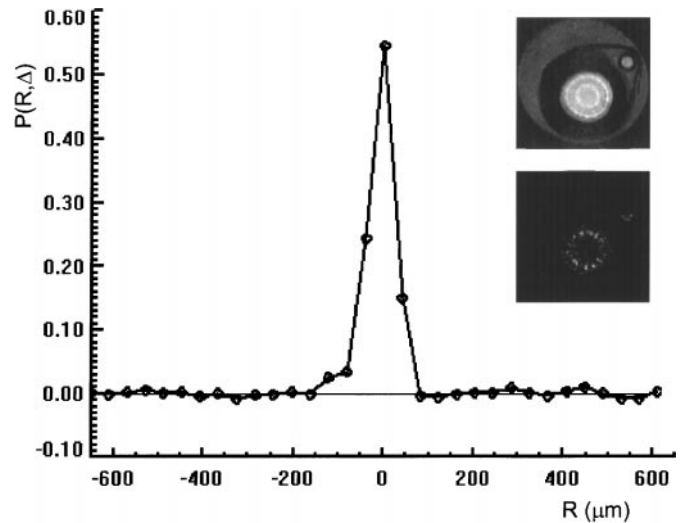

FIG. 6. The normalized averaged propagator from pixels in the xylem region of a pedicel of a tomato. The shoulder with negative displacements corresponds to water that flows with maximum linear flow velocities of 0.67 mm/s (the sign of the displacements merely indicates the direction of flow). The top image in the inset is the integral image of all displacements between -121 and $+41$ μm: a reference capillary is attached to the silicon tube (the large ring with no intensity around the pedicel) and placed in a test tube with water. The bottom image is the image at a displacement of -121 μm, showing bundles with flowing water in the xylem. Experimental parameters: 128×128 matrix; field of view, 15.0 mm; slice thickness, 4.0 mm; repetition time, 1.0 s; 32 echoes in TSE train; echo time in train, 4.4 ms; 32 PFG steps; Δ, 180 ms; δ, 2.0 ms; PFG$_{max}$, 0.144 T/m; 32 echoes; measurement time, 17 min.

FIG. 5. The distribution of the ADCs of the images presented in Fig. 4 for three different Δ values (thin line, 15.1 ms; dotted line, 100.1 ms; thick line, 400.1 ms): three histograms of the amount of pixels of the image of the maize plant stem belonging to an ADC value indicated on the x axis.

4 mm diameter) from a tomato, attached a silicone tube to the pedicel on the plant stem side and installed it in a test tube with water in the instrumental setup. A small pressure was applied to the pedicel with a water column in the silicone tube of 1.8 m (1.8 m water pressure corresponds to 17.6 kPa) to induce flow through the xylem vessels. The inset in Fig. 6 shows two images of the pedicel: the top image is the total integral of the images from displacements −121 to 41 μm from the pixel propagators, whereas the bottom image is the signal intensity at a displacement of −121 μm only (the scale of the bottom image is 15 times smaller than that of the top image). The contrast in the top image is caused by T_1: apart from T_1 delay in the time from the second to the third 90° pulse, tissue with long T_1 values will be partially saturated with the used repetition time of 1 s. In the top image different tissues in the pedicel can be distinguished: the outer ring with a low intensity is the cortex, the first bright ring is the phloem, the second ring with low intensity is the xylem, and the pith is located in the center. The bottom image only has intensity in a few bundles in the xylem: the normalized averaged pixel propagator from the corresponding pixels is the propagator in Fig. 6. Apart from the large amount of stationary water, the shoulder with negative displacements is clear: flowing water in the xylem of this pedicel has linear flow velocities up to 121 μm in 180 ms ($\approx$0.67 mm/s).

CONCLUSIONS

The successful implementation of a stimulated echo in a PFG TSE imaging pulse sequence creates the possibility of constructing propagators with observation times of several hundreds of milliseconds between the two displacement-encoding PFGs. These observation times are much longer than those that can generally be reached by PFG SE because T_1 in biological tissues is usually much longer than T_2, so sufficient signal is left for the stimulated echo and turbo spin echo train. Unwanted spurious echoes from the first three 90° pulses are successfully suppressed before the TSE part of the sequence by spoiler gradients. The use of accurate 180° pulses and an appropriate phase scheme of the 180° pulse train preserve a coherent phase in the echo train, so amplitude and phase attenuation of the PFGs are retained throughout the TSE part of the sequence. In this way a fast imaging method is combined with a quantitative measurement of the displacement distribution of water in a pixel within long observation times.

In the phantom study the long Δ values enable a clear distinction between stationary water and water flowing with a plug flow profile at a velocity as low as 50 μm/s. In a cutoff maize plant the use of a series of observation times ranging from 15 to 400 ms revealed an increasing contrast in the ADCs of different tissues: mean values of the ADC distributions decreased and ADC distribution widths increased with increasing Δ. The averaged propagator of pixels with flowing water in the xylem

region of a small tomato pedicel revealed an asymmetric shape: apart from a large amount of stationary water, flowing water with linear flow velocities up to 0.67 mm/s could also be discerned with an observation time of 180 ms. Tracking the development of ADCs of different tissues as a function of Δ (e.g., in different PFG directions for diffusion tensor measurements), together with the possibility of observing very slow flow, can make the PFG STE TSE pulse sequence a useful tool in displacement studies in different scientific disciplines.

ACKNOWLEDGMENT

REFERENCES

1. E. O. Stejskal and J. E. Tanner, *J. Chem. Phys.* **42,** 288–292 (1965).

2. P. T. Callaghan, C. D. Eccles, and Y. Xia, *J. Phys. E.* **21,** 820–822 (1988).

3. J. Kärger and W. Heink, *J. Magn. Reson.* **51,** 1–7 (1983).

4. P. T. Callaghan, W. Köckenberger, and J. M. Pope, *J. Magn. Reson. B* **104,** 183–188 (1994).

5. W. Köckenberger, J. M. Pope, Y. Xia, K. R. Jeffrey, E. Komor, and P. T. Callaghan, *Planta* **201,** 53–63 (1997).

6. T. W. J. Scheenen, D. van Dusschoten, P. A. de Jager, and H. Van As, *J. Magn. Reson.* **142,** 207–215 (2000).

7. T. W. J. Scheenen, D. van Dusschoten, P. A. de Jager, and H. Van As, *J. Exp. Bot.* **51,** 1751–1759 (2000).

8. E. Kuchenbrod, M. Landeck, F. Thürmer, A. Haase, and U. Zimmermann, *Bot. Acta* **109,** 184–186 (1996).

9. M. Rokitta, U. Zimmermann, and A. Haase, *J. Magn. Reson.* **137,** 29–32 (1999).

10. M. Rokitta, A. D. Peuke, U. Zimmermann, and A. Haase, *Protoplasma* **209,** 126–131 (1999).

11. U. Tallarek, E. Rapp, T. Scheenen, E. Bayer, and H. Van As, *Anal. Chem.* **72,** 2292–2301 (2000).

12. J. Frahm, K. D. Merboldt, W. Hänicke, and A. Haase, *J. Magn. Reson.* **64,** 81–93 (1985).

13. K. D. Merboldt, W. Hänicke, and J. Frahm, *J. Magn. Reson.* **64,** 479–486 (1985).

14. K. D. Merboldt, W. Hänicke, and J. Frahm, *J. Magn. Reson.* **67,** 336–341 (1986).

15. P. T. Callaghan, "Principles of Nuclear Magnetic Resonance Microscopy," p. 76, Clarendon Press, Oxford (1991).

16. J. Hennig, A. Nauerth, and H. Friedburg, *Magn. Reson. Med.* **3,** 823–833 (1986).

17. D. C. Alsop, *Magn. Reson. Med.* **38,** 527–533 (1997).

18. H. T. Edzes, D. van Dusschoten, and H. Van As, *Magn. Reson. Imaging* **16,** 185–196 (1998).

19. W. T. Vetterling, S. A. Teukolsky, W. H. Press, and B. P. Flannery, "Numerical Recipes Example Book (C)," p. 247, Cambridge Univ. Press, Cambridge, UK (1992).

20. P. H. Raven, R. F. Evert, and S. E. Eichhorn, "Biology of Plants," fourth ed. Worth, New York (1986).

21. D. van Dusschoten, C. T. Moonen, P. A. de Jager, and H. Van As, *Magn. Reson. Med.* **36,** 907–913 (1996).